UKAEA-CCFE-PR(21)42

Yichen Qian, Mark Gilbert, Lucile Dezerald, David Cereceda

Using first-principles calculations to predict the mechanical properties of transmuting tungsten under first wall fusion power-plant conditions

Using first-principles calculations to predict the mechanical properties of transmuting tungsten under first wall fusion power-plant conditions

Yichen Qian, Mark Gilbert, Lucile Dezerald, David Cereceda

This is a preprint of a paper submitted for publication in
Journal of Physics: Condensed Matter

Using first-principles calculations to predict the mechanical properties of transmuting tungsten under first wall fusion power-plant conditions

Yichen Qian,[1] Mark R. Gilbert,[2] Lucile Dezerald,[3] and David Cereceda[1,*]

[1]*Department of Mechanical Engineering,*
Villanova University, Villanova, PA 19085, USA

[2]*United Kingdom Atomic Energy Authority, Culham Centre For fusion Energy,*
Culham Science Centre, Abingdon, Oxon, OX14 3DB, UK

[3]*Department of Materials Science and Engineering,*
Institut Jean Lamour, Universite de Lorraine, F-54011 Nancy, France

(Dated: March 3, 2021)

Tungsten and tungsten alloys are being considered as leading candidates for structural and functional materials in future fusion energy devices. The most attractive properties of tungsten for the design of magnetic and inertial fusion energy reactors are its high melting point, high thermal conductivity, low sputtering yield and low long-term disposal radioactive footprint. Yet, despite these relevant features, tungsten also presents a very low fracture toughness, mostly associated with inter-granular failure and bulk plasticity, that limits its applications. Significant neutron-induced transmutation happens in these tungsten components during nuclear fusion reactions, creating transmutant elements including Re, Os and Ta. Density functional theory (DFT) calculations that allow the calculation of defect and solute energetics are critical to better understand the behavior and evolution of tungsten-based materials in a fusion energy environment. In this study, we perform DFT calculations to predict elastic and plastic mechanical properties (such as bulk modulus, shear modulus, ductility parameter, etc.) on a variety of W-X compositions that result when pure tungsten is exposed to the EU-DEMO fusion first wall conditions for ten years.

---

[*] david.cereceda@villanova.edu

I. INTRODUCTION

Tungsten and tungsten alloys are being considered as leading candidates for structural and functional plasma facing materials (PFMs) in future fusion energy devices. The most attractive properties of tungsten for the design of magnetic fusion energy reactors are its high melting point and thermal conductivity, low sputtering yield and low long-term disposal radioactive footprint. These advantages are accompanied unfortunately by a very low fracture toughness (mostly associated with inter-granular failure and bulk plasticity), low ductility at room temperature, and high ductile-to-brittle transition temperature (DBTT), that limits its applications [1–5].

A deep understanding of both elastic and plastic mechanical properties of tungsten alloys under first wall fusion power plant conditions is then a necessary step towards their consolidation as a viable option for this promising technology. Given the difficulty and the cost to perform experiments in such extreme environments, the use of computational modeling to provide insights and enrich the experimental knowledge of materials response has received much attention during the last decades. Among all the available techniques that allow for the prediction of mechanical properties across different temporal and spatial scales, density functional theory (DFT) has emerged as one of the most reliable ones to investigate the electronic structure of condensed matter systems [6].

In the elastic region, these first-principles calculations (also called *ab initio* calculations) have been broadly employed to study the elastic constants and the elastic properties of pure crystals and multiple alloys, starting in the 1970s and, particularly, in recent times [7–13].

For its part, plastic deformation in body-centered cubic (bcc) metals like tungsten is peculiar due to the existence of nonplanar dislocations with screw character and thermally-activated mobility [14–17]. This results in various kinds of complex phenomena such as pencil glide, asymmetry of the critical stress in the twinning and antitwinning glide directions, asymmetry of the critical stress under tension/compression loading, or anomalous slip [18–28]. Among all the mechanical properties that can be determined in this plastic regime, ductility of tungsten and tungsten alloys has been the subject of much research and discussion over the last decades (both experimentally and computationally) given their well documented brittleness [5, 29]. Despite the scalability limitations of *ab initio* methods to characterize directly dislocation glide, grain boundaries, hardening, and other mesoscopic phenomena governing the plasticity of body-centered cubic (bcc) metals, several approaches have proposed measures of ductility based on its relationship with material parameters that can be determined via DFT simulations. Going back to the 1950's, before computational modeling and *ab initio* calculations became effective methods to study the mechanical properties of materials, Pugh [30] formulated an empirical criterion that characterizes the ductility of materials by the ratio between the bulk modulus B and the shear modulus G. Cauchy pressure, defined in terms of the elastic constants, has also been employed to evaluate the ductility of metals since it includes the angular character of atomic bonding [31, 32]. Another criteria for isotropic polycrystalline materials is the Poisson's ratio, which is found to be proportional to the intrinsic ductility of crystals [33]. During analysis of dislocation nucleation from a crack tip, Rice [34] proposed that the ductile-brittle behavior of a material can be associated with the ratio between the surface energy and the so-called unstable stacking fault energy, a new solid state parameter identified in this analysis that represents the maximum energy encountered in the block-like sliding of a slip plane.

Despite the numerous efforts in the literature to investigate the effects of alloying elements on various properties of tungsten such as phase stability [10, 35–38], elastic properties [10, 13, 35–37, 39, 40], ideal tensile strength [10, 41], ductility [42], radiation defects [36], point defects [35, 43–47], dislocation structure [48, 49], grain boundaries [50], etc., to the best of our knowledge there is a lack of understanding on how the expected first wall fusion power-plant conditions change the mechanical properties of these plasma facing structural materials over time. In this work, we perform first-principles calculations based on density functional theory to investigate the mechanical response of tungsten exposed to fusion-like environments. In particular, we focus on how the elastic constants, elastic properties, ideal tensile strength, and dislocation-based ductility parameter evolve as the composition of tungsten changes during the course of irradiation due to transmutation.

Our paper is organized as follows. After this introduction, we provide an overview of tungsten transmutation in a predicted fusion-reactor environment. This is followed by Section III, where the first-principles computational methods employed are presented. The results are given in Section IV, which includes: (i) the validation exercise, with special focus on the elastic properties of pure tungsten; and (ii) the calculation of the elastic constants and elastic properties, the ideal tensile strength, and ductility parameter measurements for the chemical compositions that appear when pure tungsten transmutes during the course of irradiation. We finalize in Section V with a brief discussion and the conclusions.

II. TUNGSTEN TRANSMUTATION

To characterize the transmutation properties of W in a fusion-like environment, calculations have been carried out using the FISPACT-II inventory code developed and maintained by the United Kingdom Atomic Energy Authority over the last 30 years. FISPACT-II [51, 52] solves coupled differential equations describing the rate of change of all possible nuclides and thus evolves a nuclide composition in time. In the simplest case, the differential equation describing the rate of change for one nuclide is:

$$\frac{dN_i}{dt} = \underbrace{-N_i(\lambda_i + \sigma_i\phi)}_{\text{depletion}} + \sum_{j\neq i}\underbrace{N_j(\lambda_{ji} + \sigma_{ji}\phi)}_{\text{creation}} \qquad (1)$$

where N_i is the number of atoms of nuclide i at a given time t. This differential equation is formed from two terms that represent the nuclide depletion (negative contribution) or creation (positive). The loss term, $-N_i(\lambda_i + \sigma_i\phi)$, includes λ_i as the decay constant of the nuclide (only non-zero if the nuclide is unstable), ϕ as the total neutron flux (in units of n cm^{-2} s^{-1}), and σ_i as the total collapsed cross section for all possible reactions on the nuclide (measured in barns and calculated by combining the energy-dependent specified neutron field with nuclear reaction cross-section data). For its part, the creation term consists of the sum over all other nuclides with the ji subscripts indicating the production of nuclide i from a reaction or decay on j. Single-value, total σ cross sections (in cm^{-2} units) in equation (1) are obtained from the sum of the energy dependent cross sections values for the reaction weighted by the normalized neutron irradiation spectrum:

$$\sigma = \sum_n \sigma_n \frac{\phi_n}{\sum_m \phi_m}, \tag{2}$$

where the n, m sums are performed over the neutron flux vector.

For the present work, a $\underline{\phi}$ vector of fluxes was taken from neutron transport calculations performed for a recent conceptual design (see [53, 54] for details) for EU-DEMO; a demonstration fusion power plant being researched in Europe [55, 56]. Specifically, the spectrum for the outer equatorial first wall of the torus-shaped tokamak has been used, which is predicted to be one of the highest flux regions of a fusion reactor (second only to the inner equator). The total flux ϕ for this spectrum was 2.1×10^{14} n cm^{-2} s^{-1}. A FISPACT-II calculation evolved initially pure W in this neutron environment for 10 continuous full-power years. Figure 1(a) shows the final composition of the material after those 10 years in a 'nuclide map' [57] tableau.

Note that 10 years of continuous operation is longer than that envisaged for first wall or divertor armour components in current fusion reactor concepts; for example, EU-DEMO operational scenarios consider around 5 years of pulsed operation lifetime for divertors - corresponding to $\sim$ 2 full power years (fpy), while in the second, longer phase of EU-DEMO operation, blanket and first wall components are expected to experience about 14 years of pulsed operation ($\sim$ 6 fpy) [58]. In this respect, using the maximum transmutation results (at 10 years) presented here to analyze the mechanical impact on transmutation is an upper-bounding case relative to the end-of-life variations that might be expected in the next (first) generation of fusion reactors. On the other hand, the lesson from the nuclear fission industry is that life extension of components is critical to the commercial viability of power plants, and thus 10 fpy may eventually be more representative of the lifetime requirements for the first wall armour of commercial reactors.

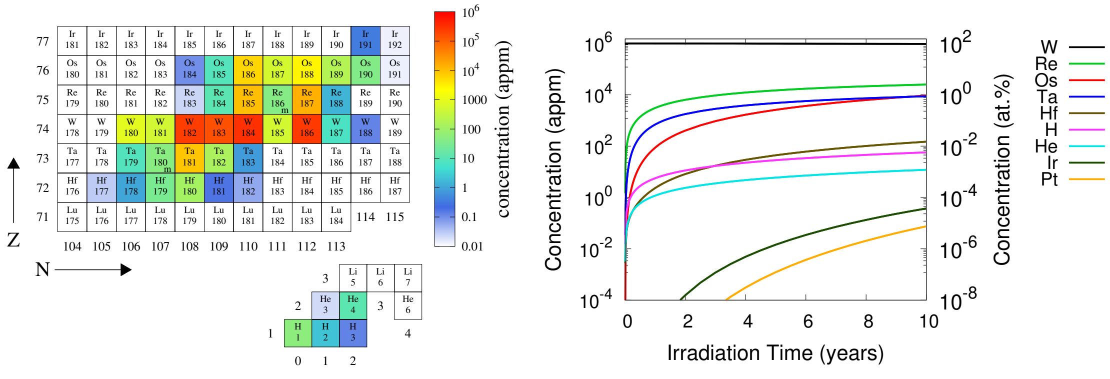

(a) (b)

Figure 1. (a) Final nuclide composition of W after 10 years of continuous exposure to EU-DEMO first wall conditions. (b) Transmutation of W during a 10-year irradiation.

Figure 1(b) shows how the composition of W changed (transmuted) during the 10-year irradiation. The graph shows the concentrations, in atomic parts per million (appm), on a logarithmic scale of the elements created during the course of the irradiation. The concentrations of each element are the sum over all nuclides of that element (i.e. from one row of the nuclide map in figure 1(a)). Table I presents the concentrations of the elements produced at 1-year intervals. The table also shows time-averaged concentration error estimates for each element, which are derived solely from the nuclear data uncertainties in the TENDL-2017 [59] libraries used by FISPACT-II to perform the calculations. FISPACT-II obtains errors for a given nuclide/isotope (e.g. ^{186}W, ^{185}Re or ^{2}H) by summing (in quadrature) the nuclear data uncertainties on each reaction in the production chains of individual nuclides N_i of the inventory. Production chains are found using a tree search

Table I. Relative concentrations that appear as W transmutes during the course of the 10-year power-plant first wall irradiation. Time-averaged % errors in transmutant concentrations predicted by FISPACT-II are also shown for each element (see main text for details).

Year	at%				appm				
	W	Re	Os	Ta	Hf	H	He	Ir	Pt
1	99.61	0.31	0.01	0.07	2.3	5.6	1.2	4.4×10^{-6}	3×10^{-8}
2	99.14	0.64	0.04	0.18	8.2	11.3	2.4	1.6×10^{-4}	3.6×10^{-6}
3	98.67	0.95	0.09	0.28	17.3	17.0	3.6	1.2×10^{-3}	5.0×10^{-5}
4	98.22	1.23	0.17	0.38	29.4	22.6	4.7	4.9×10^{-3}	3.1×10^{-4}
5	97.77	1.48	0.26	0.48	44.0	28.4	5.9	1.4×10^{-2}	1.2×10^{-3}
6	97.33	1.72	0.37	0.57	60.9	34.1	7.1	3.5×10^{-2}	3.7×10^{-3}
7	96.90	1.94	0.49	0.65	80.0	39.8	8.3	7.2×10^{-2}	9.3×10^{-3}
8	96.49	2.14	0.63	0.73	101.1	45.6	9.5	1.3×10^{-1}	2.1×10^{-2}
9	96.07	2.33	0.77	0.80	124.1	51.4	10.8	2.3×10^{-1}	4.1×10^{-2}
10	95.67	2.50	0.93	0.87	148.8	57.1	12.0	3.7×10^{-1}	7.5×10^{-2}
error (%)	0.13	6.47	7.54	36.14	31.29	12.65	42.44	31.14	37.83

algorithm (see [51] for details of the method). The errors shown here for a transmutant element are the sums (again, in quadrature) over the predicted errors for each nuclide of that element. Errors for Pt and Ir were not calculated for all time steps because the concentrations of contributing Pt/Ir nuclides were too numerically insignificant (small) for the pathways to be found – the averaged errors in these cases are only over those (later) time steps where errors were obtained

Even after 10 years and for the (relatively) highly-transmuting W, the material would still be more than 95% W. Notice that the profile of growth of each transmutant element varies – Os, for example is a secondary transmutant whose rate of production increases as the concentration of Re, a primary transmutant, increases.

III. FIRST-PRINCIPLES COMPUTATIONAL METHODS

Density Functional Theory (DFT) calculations were performed by using the open-source software distribution QUANTUM ESPRESSO [60, 61]. The generalized gradient approximation (GGA) with the Perdew-Burke-Ernzerhof (PBE) parametrization [62] was employed in the formulation of the exchange correlation functional. Optimized Norm-Conserving Vanderbilt Pseudopotentials [63] compatible with the Virtual Crystal Approximation (VCA) [64] method were chosen as the most suitable ones to study the variety of transmuted tungsten compositions that result from the exposure to the first wall conditions described in Section II. By using this VCA approach, the mixed pseudopontential for any composition at a specific irradiation time in Fig. 1(b) can be generated by defining "virtual" atoms at concentrations appropriate for the composition.

The k-points were sampled using the Monkhorst-Pack method [65] by a shifted $30 \times 30 \times 30$ grid for the 2-atom bcc supercell used in the calculation of the elastic constants and the ideal tensile strength. A shifted $28 \times 28 \times 1$ grid was selected for the 12-atom bcc supercell employed in the calculation of the stacking fault energies needed to obtain Rice's ductility parameter. The planewave cutoff energies were $\sim$ 2041 eV (150 Ry) for the elastic constants and the ideal tensile strength simulations and $\sim$ 544 eV (40 Ry) for ductility simulations. The convergence tests to choose these values are provided in Appendix A. Further details on how to extract the elastic and plastic properties of transmuting tungsten from the energies calculated via DFT simulations are given below.

A. Elastic constants and elastic properties

The change in the total energy per unit volume ($\Delta U/\Omega$) of a system subjected to a general deformation can be written, in the contracted *Voigt notation*, as

$$\frac{\Delta U}{\Omega} = \frac{1}{2} C_{ij} u_i u_j \quad \text{with} \quad u_i = \begin{cases} \epsilon_i & \text{if } i = 1, 2, 3 \\ 2\epsilon_i & \text{if } i = 4, 5, 6 \end{cases} \tag{3}$$

where Ω is the volume and U is the total energy, respectively, of the crystalline unit cell, C_{ij} are the components of the stiffness matrix, and u_i are the engineering strain vectors. In the particular case of a cubic crystal such as bcc tungsten, the elastic tensor gets simplified due to the symmetries of the lattice [66], *i.e*:

$$C_{ij} = \begin{pmatrix} C_{11} & C_{12} & C_{12} & & & \\ C_{12} & C_{11} & C_{12} & & & \\ C_{12} & C_{12} & C_{11} & & & \\ & & & C_{44} & & \\ & & & & C_{44} & \\ & & & & & C_{44} \end{pmatrix} \tag{4}$$

where all the empty entries correspond to $C_{ij} = 0$. Then, Eq. 3 can be rewritten as

$$\frac{\Delta U}{\Omega} = \frac{1}{2} C_{11}(u_1^2 + u_2^2 + u_3^2) + C_{12}(u_1 u_2 + u_1 u_3 + u_2 u_3) + \frac{1}{2} C_{44}(u_4^2 + u_5^2 + u_6^2) \tag{5}$$

Following [67–69], the three non-zero elastic constants C_{11}, C_{12}, and C_{44} can then be obtained by evaluating this Eq. 5 under three deformations: isotropic ($u_1 = u_2 = u_3 = \eta, u_4 = u_5 = u_6 = 0$), tetragonal ($u_1 = u_2 = -\eta, u_3 = -2\eta, u_4 = u_5 = u_6 = 0$), and trigonal ($u_1 = u_2 = u_3 = 0, u_4 = u_5 = 0, u_6 = \eta$), where η denotes the distortion parameter.

Since C_{11}, C_{12}, and C_{44} constitute the entire set of elastic constants for a cubic system, other elastic properties of interest for single crystals can be extracted from these energy calculations. For example, the Bulk modulus B and the tetragonal shear elastic constant C' can be determined as

$$B = \frac{1}{3}(C_{11} + 2C_{12}) \tag{6}$$

$$C' = \frac{C_{11} - C_{12}}{2} \tag{7}$$

Additionally, mechanical properties of isotropic polycrystalline materials can also be determined from the already calculated elastic constants. By applying the Hill average [70], the shear modulus G can be calculated as

$$G = \frac{G_V + G_R}{2} \tag{8}$$

where $G_V = \frac{3C_{44}+C_{11}-C_{12}}{5}$ and $G_R = \frac{5(C_{11}-C_{12})C_{44}}{4C_{44}+3(C_{11}-C_{12})}$ are the Voigt and Reuss bounds, respectively. Then the Young's modulus E and the Poisson's ratio ν can be obtained as:

$$E = \frac{9BG}{3B + G} \tag{9}$$

$$\nu = \frac{3B - 2G}{2(3B + G)} \tag{10}$$

B. Ideal tensile strength

The ideal tensile strength of a material σ_m, also called theoretical strength, is defined as the maximum stress that the material can sustain. For the uniaxial tensile test, the tensile stress σ relates to the total energy of the system U, the tensile strain ϵ, and the volume at a given strain $\Omega(\epsilon)$ as

$$\sigma = \frac{1}{\Omega(\epsilon)} \frac{\partial U}{\partial \epsilon}, \tag{11}$$

which allows for the calculation of the ideal tensile strength using first-principles simulations. To do so, the total energy for the unloaded material is firstly calculated. Second, a uniaxial tensile strain ϵ is imposed on the system, finding the minimum of the total energy by relaxing the atoms at the directions perpendicular to the loading axis. This process is repeated for different values of the strain (along the same loading direction) and the total energy is obtained as a function of the applied tensile strain. At each strain step (0.02 at the beginning and 0.01 as the results approach the region of the ideal strength), the force tolerance during the energy minimization was set to a value of 2.57×10^{-3} eV/Å (10^{-4} Ry/bohr) for all five components except for the one where the uniaxial tensile strain is applied. Eq. 11 is evaluated to calculate the stress σ for each particular strain, and the ideal tensile strength σ_m is obtained as the maximum in the stress-strain curve, which also relates to the inflection point in the total energy-strain curve [9]. Next, Eq. 11 is evaluated for each value of applied strain to determine the dependence of the stress σ with the strain. Finally, the ideal tensile strength σ_m is obtained as the maximum in the stress-strain curve, which also relates to the inflection point in the total energy-strain curve [9].

C. Dislocation-based ductility parameter

According to the dislocation theory formulated by Rice [34], the brittle-ductile behavior of a crystalline solid can be characterized by the so-called ductility parameter D that accounts for the competition between the nucleation of dislocations from the crack tip and crack cleavage, *i.e.*:

$$D = \frac{\gamma_s}{\gamma_{us}} \tag{12}$$

where γ_s is the surface energy and γ_{us} is the unstable stacking fault energy. In the present work, we focus on this Rice-criterion of ductility instead of the other three criteria described in Section I since the generalized stacking fault energies (GSFE) that are needed in Eq. 12 can be determined directly by using first-principle simulations. Additionally, the calculation of the GSFE could also provide physical insights into the movement of dislocations, a mechanism that governs plastic deformation in bcc metals like tungsten [71–74].

The first step in the calculation of the GSFE is the definition of the geometry. A supercell containing twelve surface layers with a unit surface of 1 × 1 and 10 (Å) vacuum is created as shown in Fig. 2. This is done for both $\langle 1\,1\,1\rangle\{\bar{1}\,1\,0\}$ and $\langle 1\,1\,1\rangle\{1\,1\,\bar{2}\}$, the two primary slip systems found in these bcc structures [75–78]. Next, a displacement along the $[1\,1\,1]$ direction is imposed on the upper half (7th to 12th layers) of the surface model while keeping the lower half (1st to 6th layers) fixed. After introducing the slip, the entire system is allowed to relaxed along the z direction. The GSFE (also called γ-surface) is then defined as the energy cost per unit area of the cut incurred as a result of the shift, *i.e.*:

$$\gamma(x) = \frac{E(x) - E_0}{A} \tag{13}$$

where x is the displacement along the shift vector (given as a fraction of the Burgers vector $\mathbf{b} = \frac{1}{2}\,[1\,1\,1]$), $E(x)$ is the total energy of the system after imposing a slip x, E_0 is the total energy of the surface model before the slip, and A is the area of the surface. The unstable stacking fault energy γ_{us} is obtained as the maximum value of the GSFE curve and it corresponds to the maximum energy that comes upon sliding the top half along a slip plane [34].

For its part, the surface energy γ_s is the energy required to create a new surface during the cleavage of an infinite crystal in two. Despite its importance to understand surface structure, reconstruction, roughening and crystals' equilibrium shape [79], there are some challenges to determine it both experimentally [80] and computationally [81]. In this work, we use the method proposed by Fiorentini and Methfessel [82] that calculates the surface energy as

$$\gamma_s \approx \frac{E_{slab}^{N} - NE_{bulk}}{2} \tag{14}$$

where E_{slab}^{N} is the total energy of an N-layer slab and E_{bulk} is the bulk total energy. By using this approach, the divergence of the surface energy with the slab thickness is eliminated. Additionally, it does not require the calculation of the bulk energy term on a separate system since E_{bulk} can be taken as the slope of the total energy of the slap over the slap thickness.

IV. RESULTS

In this Section, we present results of first-principles calculations to explore the dependence of the elastic constants, ideal tensile strength, and ductility-parameter on the time-dependent composition of transmuting tungsten under first wall fusion power-plant conditions.

A. Benchmarking - pure tungsten

As a preliminary step in our calculations, the elastic and plastic properties of pure tungsten were obtained and compared with previous works in the literature. Table II summarizes the lattice parameter, elastic constants and elastic properties from this work

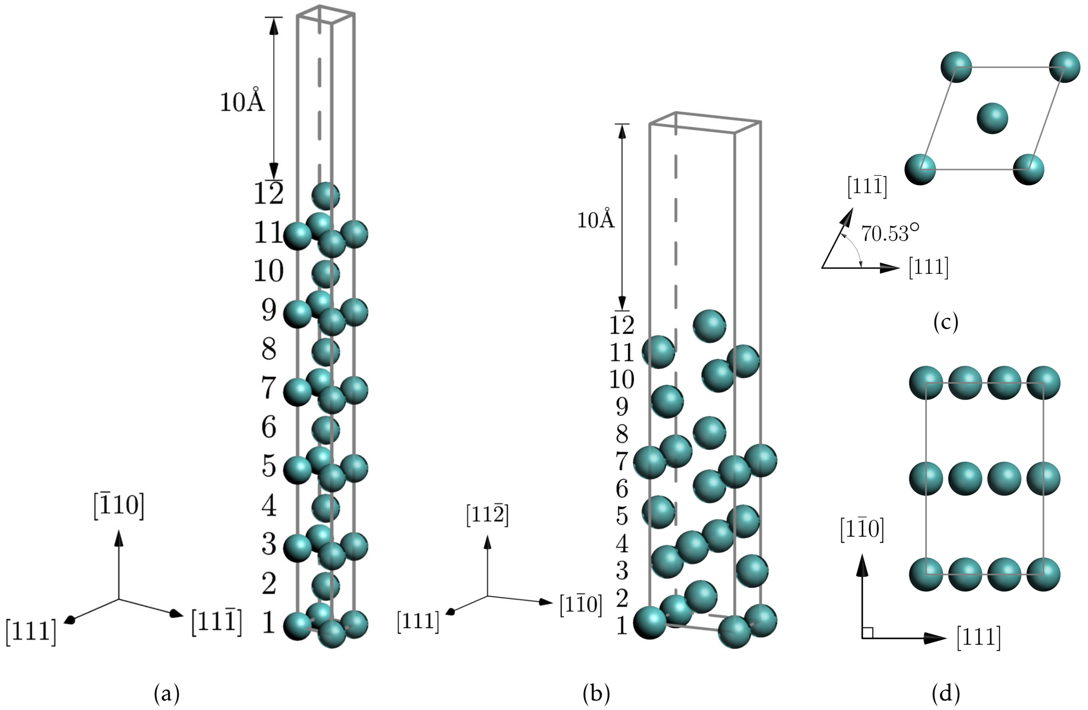

Figure 2. Atomic arrangement of the surface models used to calculate γ_{us} of transmuting tungsten on both (a) $\langle 1\,1\,1\rangle\{\bar{1}\,1\,0\}$ and (b) $\langle 1\,1\,1\rangle\{1\,1\,\bar{2}\}$ slip systems.

and previous studies. For their part, the values of the ideal tensile strength σ_m, the surface energy γ_s and unstable stacking fault energy γ_{us} are shown in Table III. These results are consistent with their counterparts from previous works (the relative differences are less than 15% in Table II and less than 12% in Table III). Additionally, given the variety of methods compared, convergence studies were also performed on several properties of interest. The reader is referred to appendix A for more details about these convergence tests.

Table II. Theoretical and experimental equilibrium lattice parameters a_0, bulk modulus B, elastic constants C_{ij}, tetragonal shear modulus C', shear modulus (G) and Young's modulus (E) of pure tungsten from our calculations and previous works.

Software package, Pseudopotential†	a_0 (Å)	C_{11} (GPa)	C_{12} (GPa)	C_{44} (GPa)	B (GPa)	C' (GPa)	G (GPa)	E (GPa)
EMTO, PAW [83]	3.195	536.7	179.9	168.6	298.8	178.4	172.5	434.0
QE, NCPP [84]	3.187	499‡	201‡	149	300	160	154‡	394‡
VASP, PAW [85]	3.1755	529.94	211.19	140.59	317.44	159.38	148.11	384.52
VASP, PAW [86]	3.17	536.3	202.2	138.7	313.6‡	167.1‡	149.4‡	386.8‡
QE, USPP [87]	3.1903	518	197	141	304	160	160 ‡	408 ‡
Exp. (0 K) [88]	3.165	532.55	204.95	163.13	314.15	163.80	163.40	417.76
Exp. (300 K)	-	530.25	201.9	160.92	311.35	164.18	160.18	410.09
QE, NCPP [This work]	3.1835	512.501	197.906	142.461	302.771	157.298	148.22	382.669
	[6%]	[5%]	[6%]	[15%]	[5%]	[12%]	[14%]	[12%]

† Acronyms used for software packages and pseudopotentials: Exact Muffin-Tin Orbitals (EMTO) formalism [89], Projector Augmented Wave(PAW), Norm Conserving pseudopotentials(NCPP), Ultra-Soft pseudopotentials(USPP).

‡ Values are obtained by substituting the elastic constants calculated via first-principles calculations into Eq. 6 – 9.

B. Elastic behavior of transmuting tungsten

With the confidence conferred by the benchmarking exercise of pure tungsten, next we proceed to calculate the elastic and plastic properties for a number of tungsten compositions that result during the first ten years of continuous exposure to EU-DEMO first wall conditions. The chemical compositions of transmuted tungsten shown in Fig. 1(b) and Table I were used to generate the required pseudopotentials via the VCA method

Table III. Theoretical ideal tensile strength σ_m, corresponding strain ϵ_m , surface energy γ_s, and unstable stacking fault energy γ_{us} of pure W from our calculations and previous works.

Software package, Pseudopotential†	σ_m(GPa)	ϵ_m(%)	$\{\bar{1}\,1\,0\}$ slip system		$\langle 1\,1\,1\rangle\{1\,1\,\bar{2}\}$ slip system	
			γ_s (J/m^2)	γ_{us}(J/m^2)	γ_s(J/m^2)	γ_{us}(J/m^2)
CPMD, GTH [9]	26.7	11.7	-	-	-	-
QE, PAW [10]	29.6	14	-	-	-	-
VASP, PAW	29.1 [86]	14 [86]	3.181[42]	1.633 [42] 1.6983[90]	3.367[42]	1.830[42] 1.7464[90]
VASP, PAW[91]	-	-	3.197	∼1.680	∼3.377	∼1.764
QE, NCPP [this work]	27.763[6%]	14[19%]	3.3083[4%]	1.6870[3%]	3.7620[12%]	1.8755[7%]

† Acronyms used for software packages and pseudopotentials: Car–Parrinello Molecular Dynamic (CPMD) code [92], Goedecker-Teter-Hutter pseudopotentials [93].

[64]. In addition to studying the current composition (i.e. all transmutants in table I) at each irradiation time, two other scenarios were considered: (i) chemical composition at each irradiation time with tungsten and the primary transmutant (Re); (ii) chemical composition at each irradiation time with the top 3 transmutants (Re, Os, Ta). The purpose of investigating these two supplementary scenarios is to understand how the mechanical properties change as specific transmutants are added.

Figure 3 shows the time dependence of the lattice parameter and the elastic constants as the chemical composition of the tungsten-based materials change due to irradiation. This linear behavior has been confirmed in previous experimental [94] and computational [10, 48] measurements of W-Re alloys.

In Figure 4 we provide detailed results on the evolution of elastic properties such as the Bulk modulus B, the tetragonal shear elastic constant C' and mechanical properties of polycrystalline materials like the shear modulus G and the Young's modulus E. As described in Section III A, the above properties can be obtained directly from relations between elastic constants, by applying the Hill average, or by imposing Voigt and Reuss

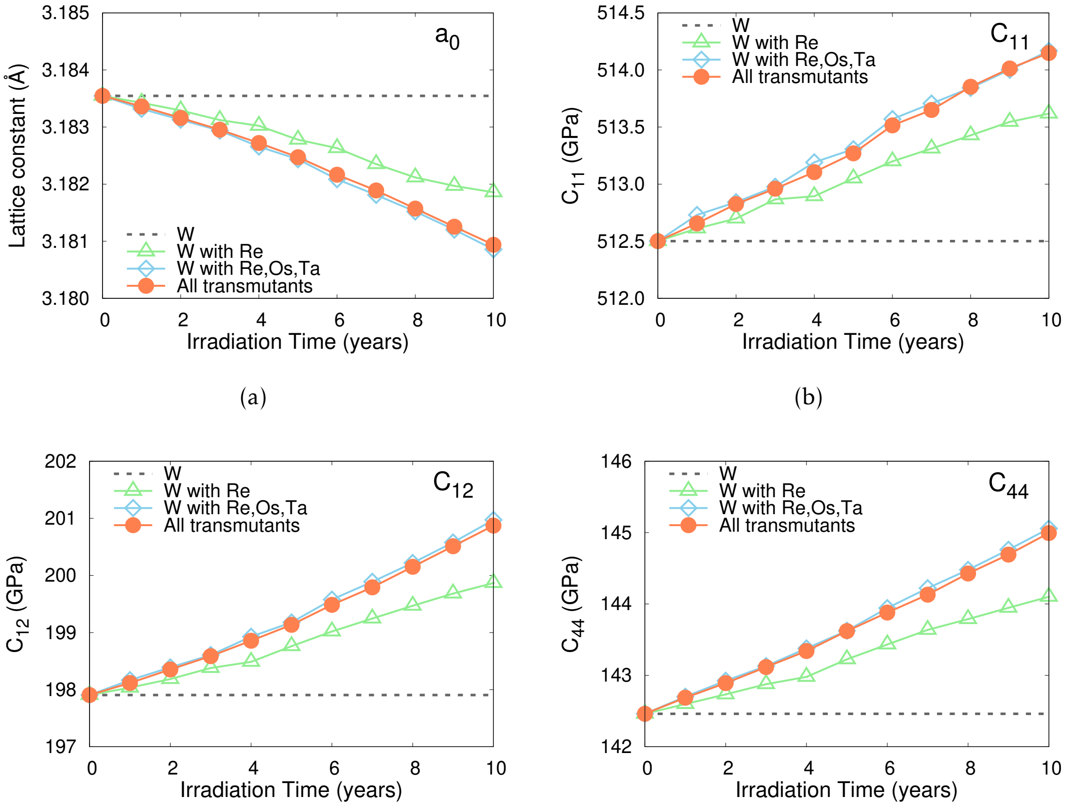

(a) (b)

(c) (d)

Figure 3. Evolution of the equilibrium lattice parameter a_0 and the elastic constants C_{ij} of transmuting tungsten during the first ten years of continuous exposure to EU-DEMO first wall conditions.

bounds. The monotonic behavior observed in our calculations is also in agreement with previous computational works that studied W-Re alloys [10].

In advance of discussing these results and their implications in detail in the following section, we note the following features from the figures: (i) the lattice constant and C' are the only measurements decreasing as irradiation time (and therefore the relative concentration of transmutants) increases. All other properties monotonically increase with irradiation time; (ii) the magnitude of the slope when only the primary transmutant (Re) is

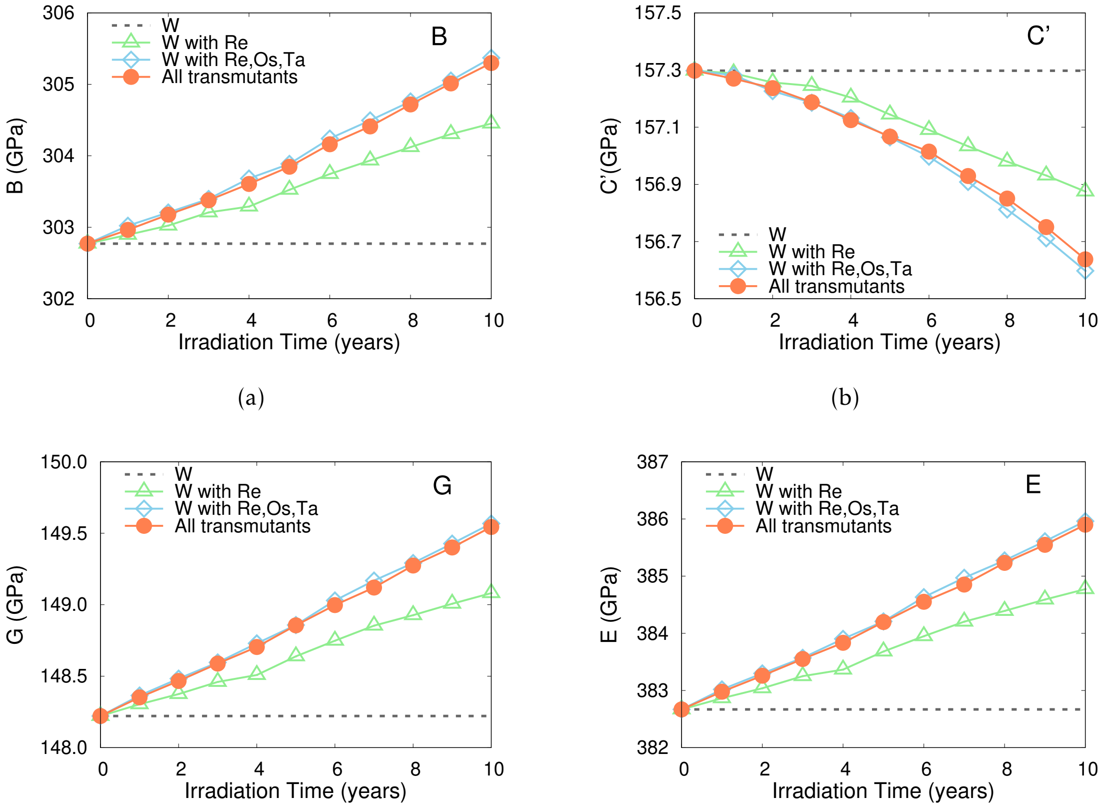

(a)

(b)

(c)

(d)

Figure 4. Evolution of the bulk modulus B, tetragonal shear modulus C', shear modulus (G), and Young's modulus (E) of transmuting tungsten during the first ten years of continuous exposure to EU-DEMO first wall conditions.

considered, (no matter whether it is positive for some properties and negative for others) is always smaller than the one for the current composition with all transmutants or the scenario that includes the top 3 transmutants; and (iii) the effect of adding all remaining transmutants is negligible when compared with the impact of the chemical compositions that includes the top 3 transmutants (Re, Os, Ta).

C. Ideal tensile strength of transmuting tungsten

The stress-strain curve is one of the most fundamental tools to understand the mechanical behavior of materials. It reveals many of the elastic and plastic properties of interest, including but not limited to Young's modulus, yield strength, ultimate tensile strength, etc. Here we perform a systematic study of the ideal tensile strength of pure W, transmuting W (with all transmutants), W with primary transmutant (Re) , and W with top 3 transmutants (Re, Os, Ta) as a function of the chemical compositions that result when pure tungsten is exposed to the EU-DEMO first wall conditions for ten years. While studying the effect of temperature on the stress-strain curve is outside the scope of this paper, it is still of interest to calculate the theoretical ideal tensile strength of transmuting tungsten in its ground state and relate our findings to the larger mechanical behavior of these candidate materials if possible.

First, we study the stress-strain relations of these materials as we increase the irradiation time. By way of example, the results for the chemical composition of transmuting tungsten that appears by the sixth year of irradiation are presented in Fig. 5(a). These reveal that the overall stress-strain curve drops as the number (and amount) of transmuting elements increases. Next, we analyze the impact on the ideal tensile strength σ_m, defined as the maximum in the stress-strain curve. The inset of Fig. 5(a) shows that while σ_m also decreases with the presence of transmuting elements, the related strain ε_m for which σ_m is achieved remains constant and $\sim$14% for all the chemical compositions studied. Figure 5(b) summarizes the evolution of σ_m during the first ten years of irradiation in increments of one year. As the figure shows, σ_m monotonically decreases with the irradiation time for all the scenarios considered. This is consistent with previous works that studied the ideal tensile strength of tungsten and tungsten alloys by first-principles calculations [10, 41]. Furthermore, adding all transmutants results only in a slight deviation from the chemical compositions that includes the top 3 transmutants (Re, Os, Ta). The observed higher values of σ_m for W including primary transmutant (Re) with respect to all-transmutants composition also aligns with the results obtained when studying the elastic behavior of transmuting tungsten, where the magnitude of the slope for W with primary transmutant was always smaller than the one for the current composition with all transmutants.

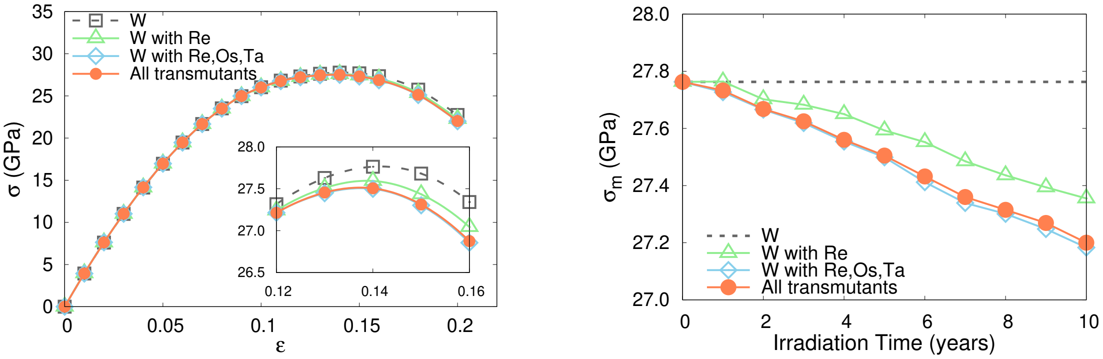

(a)

(b)

Figure 5. (a) The stress-strain curves under [001] tensile strain after six years of irradiation. (b) Evolution of the ideal tensile strength of transmuting tungsten during the first ten years of continuous exposure to EU-DEMO first wall conditions. These calculations are performed in their ground state and therefore they can not be compared directly to experimental stress-strain curves.

D. Dislocation-based ductility parameter of transmuted tungsten

In this section, we investigate the effect of transmuting elements on the ductility parameter of tungsten for $\langle 1\,1\,1\rangle\{\bar{1}\,1\,0\}$ and $\langle 1\,1\,1\rangle\{1\,1\,\bar{2}\}$ slip systems. We decided to focus here on pure W, the chemical composition that includes only the primary transmutant (Re), and the chemical composition that includes all transmutants. This choice is justified by (i) the increased computational cost to calculate γ_{us} (the reader is referred to appendix A for more details about the convergence tests shown there), and (ii) the small variations observed when studying the elastic properties and the ideal tensile strength of the chemical composition including top 3 transmutants (Re, Os, Ta) and the chemical composition with all the transmutants.

As noted in Section III C, the dislocation-based ductility parameter D formulated by Rice [34] can be obtained in terms of the surface energy γ_s and the unstable stacking fault energy γ_{us}. Next, we describe the results obtained when calculating each of these measurements, as well as the resultant ductility parameter.

γ_{us} is defined as the maximum value of the generalized stacking fault energy(GSFE) curve. As such, we need to calculate the GSFE curve for each of the chemical compositions and irradiation times considered. Figures 6(a) and 6(b) show the obtained GSFE curves of both $\langle 1\,1\,1\rangle\{\bar{1}\,1\,0\}$ and$\langle 1\,1\,1\rangle\{1\,1\,\bar{2}\}$ slip systems for the chemical compositions that results after irradiating pure tungsten at fifth year. The figures reveal several interesting trends that are consistent with previous works in the field. Firstly, γ_{us} is always in the middle of the energy path from one equilibrium position to another on a $\{\bar{1}\,1\,0\}$ plane while there is certain asymmetry towards the first equilibrium position on a $\{1\,1\,\bar{2}\}$ plane [42, 78, 91, 95]. Secondly, adding transmuting elements lowers γ_{us} of both slip systems [13, 37, 96]. Thirdly, γ_{us} is higher for the $\langle 1\,1\,1\rangle\{1\,1\,\bar{2}\}$ slip system [36, 42, 87, 91, 95]. The evolution of γ_{us} for both slip systems during the first ten years of irradiation is summarized in Fig. 6(c) and 6(d). These results show higher values of γ_{us} of the $\langle 1\,1\,1\rangle\{1\,1\,\bar{2}\}$ slip system over the entire time domain, and a monotonic decrease of γ_{us} as the irradiation time (and therefore the amount of transmuting elements) increases.

For its part, the calculation of γ_s in terms of the chemical composition and the irradiation time requires a preliminary step: the confirmation that γ_s does not diverge with increasing slab thickness [82, 97]. Following the method proposed by Fiorentini and Methfessel [82], Fig. 7(a) shows the calculated surface energies as a function of the slab thickness for the chemical compositions (all transmutants) that appear after 4 years of irradiation in tungsten. It can be seen from these results that convergence of γ_s is achieved with increasing the number of layers and a slab thickness of 12 layers assures a relative

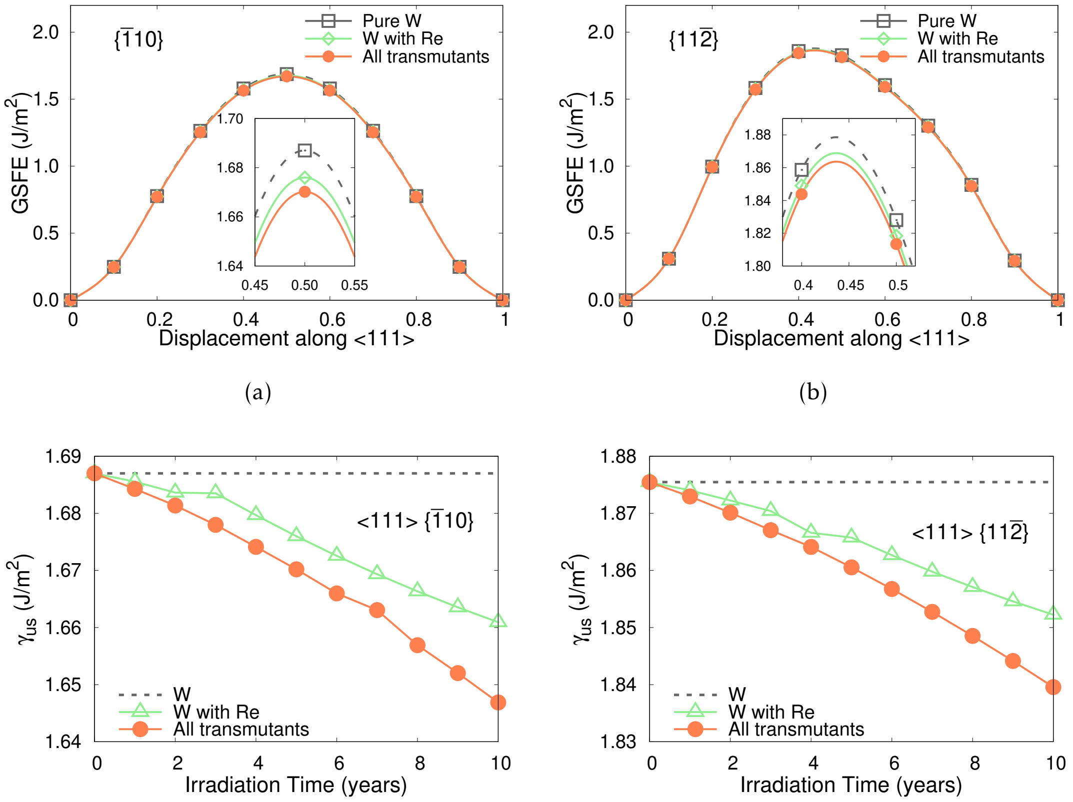

(a) (b)

(c) (d)

Figure 6. The general stacking faults energy for the slip along $\langle 111\rangle$ direction in (a) $\{\bar{1}\,1\,0\}$ and (b) $\{1\,1\,\bar{2}\}$ plane after 5 years of irradiation. Evolution of the unstable stacking fault energy γ_{us} for pure tungsten and transmuting tungsten during the first ten years of irradiation under EU-DEMO first wall conditions for both (c) $\langle 1\,1\,1\rangle\{\bar{1}\,1\,0\}$ and (d) $\langle 1\,1\,1\rangle\{1\,1\,\bar{2}\}$ slip systems.

difference of less than 0.02%. With the confidence conferred on our approach by the convergence tests, next we proceed to calculate the surface energy for a number of chemical compositions, irradiation times, and both slip systems. The results are summarized in Fig. 7(b). Despite the higher values of γ_s for the $\langle 1\,1\,1\rangle\{1\,1\,\bar{2}\}$ slip system, there is a small variation in terms of the chemical composition and the irradiation time studied, specially when compared with the evolution of γ_{us} shown in Fig. 6(c) and 6(d).

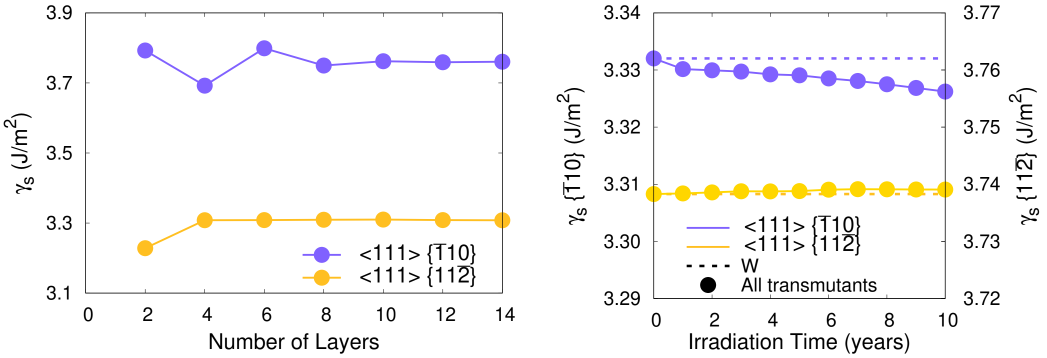

(a)

(b)

Figure 7. (a) Calculated surface energies for transmuting tungsten (all transmutants) as a function of the slab thickness after four years of irradiation; (b) Evolution of the surface energy for pure tungsten and transmuting tungsten during the first ten years of irradiation under EU-DEMO first wall conditions for both $\langle 1\,1\,1\rangle\{\bar{1}\,1\,0\}$ and $\langle 1\,1\,1\rangle\{1\,1\,\bar{2}\}$ slip systems.

Once both γ_s and γ_{us} are calculated in terms of the chemical composition and the irradiation time, the ductility parameter D is obtained by substituting these terms into Eq. 12. We present results for the two slip systems of interest in Figure 8, where the linear dependency with irradiation time is clearly distinguished. It can also be observed that D is higher on the $\langle 1\,1\,1\rangle\{1\,1\,\bar{2}\}$ slip system and the positive impact of adding more transmuting elements for a given irradiation time. This is in agreement with the well accepted improvement of the ductility of W when adding Re [36, 42, 87, 91, 95, 98].

V. DISCUSSION

A. Nuclear transmutation

Section II presented typical transmutation results for pure W in a fusion reactor first wall (plasma-exposed) environment. While tungsten is a relatively highly transmuting element (for example, compare the relative burn-up of W to other elements in figure 6

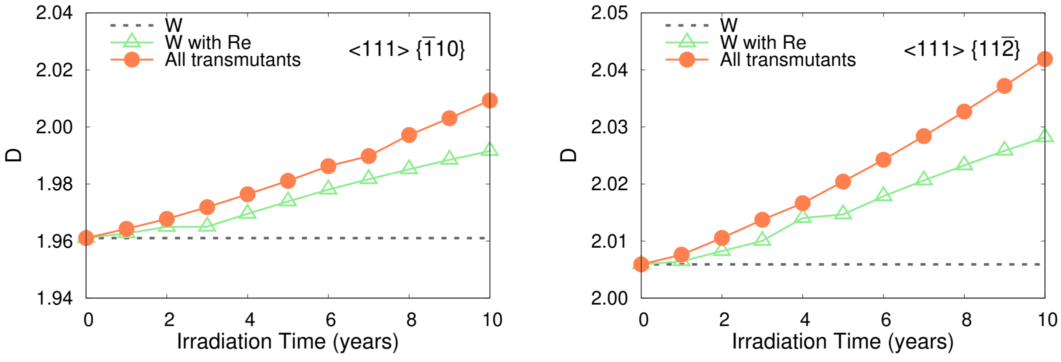

(a) (b)

Figure 8. Evolution of the ductility parameter D for transmuting tungsten along the (a) $\langle 1\,1\,1\rangle\{\bar{1}\,1\,0\}$ and (b) $\langle 1\,1\,1\rangle\{1\,1\,\bar{2}\}$ slip systems during the first ten years of continuous exposure to EU-DEMO first wall conditions.

of [99]), figure 1(b) and table I showed that W will remain relatively pure even after 10 years of exposure, with only 4-5 atomic % of transmutation impurities. However, even at such low concentrations, transmutants such as Re, Os, and Ta could still have significant impact on the engineering performance of W-based components in fusion systems. For example, 5 % Re in tungsten can cause a 10-20% reduction in the thermal diffusivity (and hence thermal conductivity) [100]. In a first wall fusion reactor having such a large variation of thermal performance in armour (where W is the preferred choice) would pose an engineering design challenge.

Even more problematic for the engineering of fusion components is uncertainties in predictions associated with nuclear response. In the present work, we have shown a rare attempt to quantify uncertainties in transmutation predictions – in codes such as FISPACT-II [51] uncertainty quantification (UQ) is typically focused on radiological responses, which is clearly important as safety margins must be well understood to plan maintenance, handling, and dismantling operations where human workers may be involved. However, where mechanical, structural, and thermal behaviour may be impacted by the complete burn-up (transmutation) response (i.e. not merely from the typically small concentrations of radioactive products of nuclear reactions) it will be vital to provide UQ for the complete inventory evolution response.

The calculations performed in this work showed errors on the main transmutation products (Re and Os) of less than 10 %, which is reasonable and typical of errors originating purely from nuclear data – see, for example, [101, 102], where decay-heat predictions by FISPACT-II for important fusion materials show good agreement with experimental measurements and where the computational errors generally generally encompass the experimental values. However, the errors shown in table I, are not the complete picture - full UQ for the results would require, in addition to the errors originating from the nuclear data used in the inventory simulations, assessment of the errors associated with the neutron transport simulations used to generate the neutron spectrum.

In the present, the spectrum comes from a neutron transport simulation (performed using MCNP [103]) of highly conceptualized model for EU-DEMO [55, 56]. As well as the errors inherent in the neutron transport simulations, which originates from the same nuclear data used for the inventory simulations with FISPACT-II, there is the unquantified – and likely quite large – uncertainty in the fusion reactor model itself.

A key challenge for the future development of fusion, which will never have the wealth of experimental devices afforded the fission industry during its development, is to assess these engineering uncertainties, perhaps using Monte-Carlo-based sensitivity studies on the reactor design parameters or otherwise.

B. Effects of transmutant elements on the mechanical properties

In Sections III A - III C we have provided calculations of the lattice parameter, elastic behavior, ideal tensile strength, and ductility parameter as new transmutant elements are added to the initial composition of pure tungsten due to irradiation. Furthermore, to better understand the effect of the most predominant elements produced in W under fusion-neutron irradiation, we also studied chemical compositions corresponding W with transmutant Re (W-Re) and also with Re, Os, and Ta (W-Re-Os-Ta) for each irradiation time. Here we consider the most important implications of the above calculations.

The results shown in Fig. 3 and Fig. 4 reveal that the lattice constant a_0 and the tetragonal shear modulus C' are the only two elastic measurements decreasing with increasing the amount of transmutant elements. These effects are closely related to the variation of the number of valence electrons per atom. For example, the reduction of the lattice constant (for a given irradiation time) with increasing the amount of transmutant elements is in agreement with experimental measurements and *d*-band filling predictions [94]. The decrease of C' with increasing impurity elements also suggests how transmuting tungsten becomes structurally unstable as the number of valence electrons increases. If we analyze the effect on other elastic constants and properties such as C_{11}, C_{44}, and E, their growth with increasing the solid solute concentrations and the number of valence electrons is in agreement with previous experimental [94] and computational works [10, 13, 87, 104]. When evaluating the quantitative effects of the chemical composition on the elastic behavior, the small amounts of impurity elements that appear due to transmutation (cf. Table I) justify the smooth change of all these elastic parameters (the maximum difference observed is 1.8% for C_{44} after 10 years of irradiation). Still, it is noticeable the major qualitative role that Re plays in the evolution of the elastic behavior, compensating the effect of other transmutant elements like Ta that decrease the number of valence electrons [10, 104]. Finally, it can be observed from these figures that the effect of burn-up creating impurity elements with a relative concentration ≤ 0.87 at.% is negligible. This has computational consequences as adding extra elements significantly increases the computational cost of the simulations.

For its part, the variability of the ideal tensile strength shown in Fig. 5(a) can be explained by investigating the electronic structures of the chemical compositions compared. When Group-VI transition metals like tungsten are deliberately alloyed with elements with more valence electrons like Re or if those elements grow-in due to transmutation, the elastic shear instability is hindered by the Jahn-Teller distortion [105]. The result is a material that presents a slightly lower ideal tensile strength when compared to the pure element, as it is shown in the aforementioned figure. This is in fact consistent with previous experimental and computational works that describe how the peak stress of W-Re alloys are lower than the corresponding values of pure W [10, 104, 106–108]. Furthermore, similarly to the observations when studying the elastic behavior of transmuting tungsten, the small variations of the ideal tensile strength for a given irradiation time when adding Hf, H, He, Ir, and Pt can be explained by the small relative concentrations of these elements (always ≤ 0.87 at.%) that appear during the course of the 10-year power-plant first wall irradiation.

Another important physical aspect of mechanical deformation in bcc crystals is their ductility. As described in Section III C, the Rice criterion [34] was chosen to estimate the ductility of transmuting tungsten. As such, the dependence of both γ_{us} and γ_s with respect to the chemical composition needs to be investigated prior to the calculation of the dislocation-based ductility parameter D (cf. Eq. 12). Several features can be discussed from these results, shown in Figs. 6 and 7. Firstly, the value of γ_{us} for each chemical composition on the $\langle 1\,1\,1\rangle\{\bar{1}\,1\,0\}$ slip system is always smaller than its counterpart on the $\langle 1\,1\,1\rangle\{1\,1\,\bar{2}\}$ slip system (cf. Fig. 6(a) and 6(b)). This suggests, confirming the findings in previous works [77, 109], that slip should predominantly occur on $\{\bar{1}\,1\,0\}$ planes. Secondly, the addition of transmuting elements decreases γ_{us}. Previous works have shown a different behavior depending on the number of valence electrons of the add-elements. Adding elements with more valence electrons than W (such as Re, Os, It, Pt) have consistently reduced γ_{us} [42, 107] while adding elements with less valence electrons than W (such as Ta, Ti, Nb, Hf) tend to slightly increase it [42, 107]. However, when comparing the value of γ_{us} in pure W, W-Re and the chemical composition with all transmutants, we observe that the addition of elements always make γ_{us} to shrink. On this basis, we find that the higher relative concentration of Re with respect to other transmutants (cf. Table I) plays a crucial role here, hindering the effect that other transmutant elements with less valence electrons than W should have.

Additionally, the results shown in Fig. 7(b) reveal that γ_s on the $\langle 1\,1\,1\rangle\{\bar{1}\,1\,0\}$ slip system is also smaller than its counterpart on the $\langle 1\,1\,1\rangle\{1\,1\,\bar{2}\}$ slip system. Still, the limited variability of γ_s with the chemical composition as irradiation time increases implies that the main factor governing the dependence of D with the chemical composition is γ_{us}. Connecting the above observations regarding γ_{us} and γ_s, the results shown in Fig. 8 indicate that, for a given chemical composition, the ductility parameter is higher as the amount of transmutants is increased. This suggests that the addition of Re (which significantly decreases γ_{us} for a relatively constant γ_s) is the main factor responsible for this increment in the ductility.

C. Evolution of the mechanical properties with irradiation time

Previous works in the literature have extensively studied the effects of alloying elements on various properties of tungsten such as phase stability [10, 35–38], elastic properties [10, 13, 35–37, 39, 40], ideal tensile strength [10, 41], ductility [42], radiation defects [36], point defects [35, 43–47], dislocation structure [48, 49], grain boundaries [50], etc. However, to the best of our knowledge, there is a lack of understanding on how the expected first wall fusion power-plant conditions change the mechanical properties of these structural materials over time. Furthermore, most of these works have studied the effects when adding single or a reduce number of alloying elements to tungsten. In this work we address this gap by investigating not only the time dependence of the mechanical properties but also the effect of adding a combination of all the elements that appear due to transmutation. Our primary observation from the results shown in Figs. 3, 4, 5(b), 7(b), and 8 is that the time evolution of the mechanical properties is governed by the characteristics of the transmutant element with the highest relative concentration.

As described in Table I, this corresponds to Re, an element with more valence electrons than W. The mechanical properties that monotonically increase when Re is added also increase as the exposure to first wall conditions continues, and vice versa. This effect (either increasing or decreasing the specific property) is slightly augmented when all the transmutants are considered, but the trend is governed by the primary transmutant element, no matter whether the other transmutants actually increase or decrease the number of valence electrons. However, we issue this conclusion with caution, as the relative concentrations of the deliberately added alloying elements in other candidate materials such as tungsten-based high-entropy alloys [110] are more similar and their mechanical behavior is expected to be different.

VI. CONCLUSIONS

To summarize, we have used the FISPACT-II inventory code to calculate how the chemical composition of pure W changed when exposed to the EU-DEMO fusion first wall conditions for ten years. We have also performed first-principles calculations to characterize how the elastic constants, elastic properties, ideal tensile strength, unstable stacking fault energy, surface energy, and ductility parameter evolve as new transmutant elements are added to pure W due to transmutation.

Our first conclusion from these investigations is that W will remain relatively pure even after 10 years of exposure to first wall fusion conditions, with only 4-5 at.% of transmutant elements. Secondly, we have observed that the effects of these transmutant elements on the mechanical properties of transmuting tungsten is closely related to the relative variation of the number of valence electrons per atom as the composition changes. In particular, we find that the relative difference of these valence electrons created by the most predominant transmutant element (Re), has an important influence all the properties calculated. Furthermore, the impact of minor transmutants (those with a relative concentration ≤ 0.87 at.%) seems negligible. Finally, our analysis of the mechanical properties as exposure to first wall fusion conditions continues over time also suggests that Re plays an important role in the evolution of the mechanical properties, increasing for example the Young's modulus, shear modulus, bulk modulus, and the ductility parameter; and decreasing the lattice constant, tetragonal shear elastic constant, ideal tensile strength, and the unstable stacking fault energy.

ACKNOWLEDGMENTS

This work used the Extreme Science and Engineering Discovery Environment (XSEDE), which is supported by National Science Foundation grant number ACI-1548562. Specifically, YQ and DC acknowledge support from XSEDE allocations MSS190015 and MAT200015. YQ and DC also acknowledge computer time allocations at Villanova's HPC-CoE cluster. MRG acknowledges funding from the RCUK Energy Programme [grant number EP/T012250/1].

Appendix A: Convergence of the DFT calculations

Figures 9 and 10 show the convergence of the lattice parameter, elastic constants, and elastic properties with respect to the plane-wave energy cutoff and the k mesh. These results suggest that an energy cutoff of 150 Ry and a 30×30×30 k-point mesh are sufficient to perform our first-principles calculations of the elastic behavior.

The convergence of the unstable stacking fault energy γ_{us} with respect to the energy cutoff, k mesh and slab size is shown in Fig. A.11. First, we studied the convergence of γ_{us} with respect to the energy cutoff and k points, keeping a fixed slab structure of 8 layers. In Fig. A.11(a) the k-points were sampled using a fixed 16×16×1 grid, being the energy cutoff the only parameter allowed to change. The results show that an energy cutoff of 40 Ry turns out to be sufficient, specially considering the computational cost and the number of GSFE calculations needed. In Fig. A.11(b) we did the opposite, fixing the energy cutoff

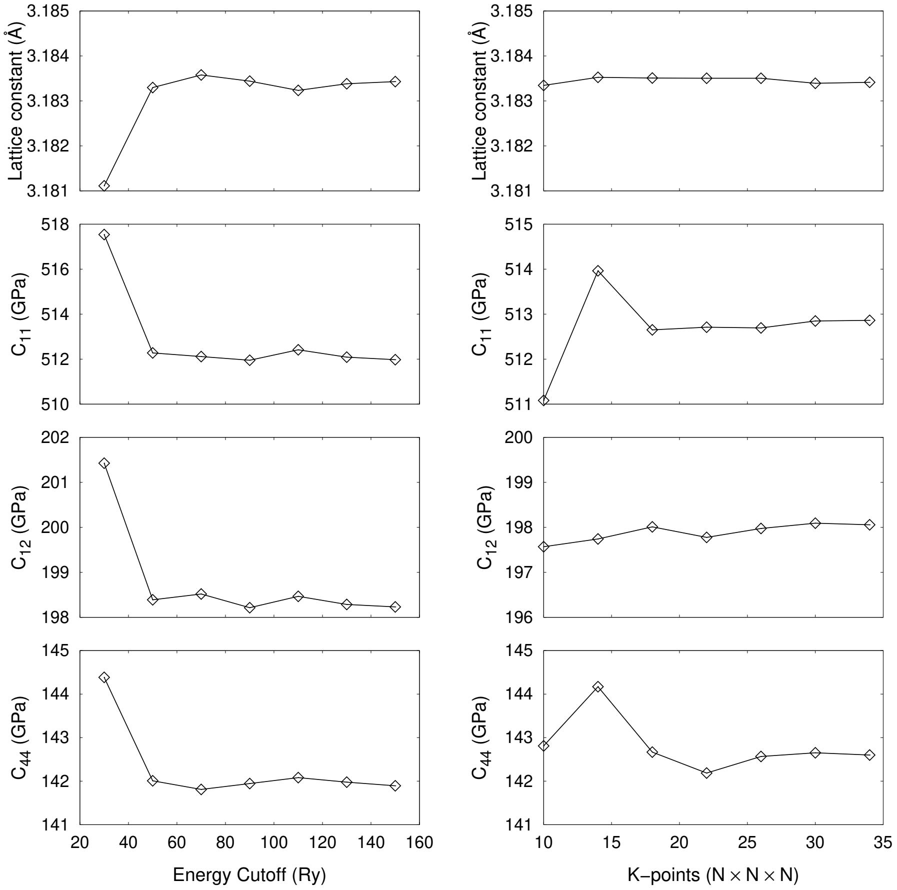

(a) (b)

Figure 9. Convergence of the lattice constant and elastic constants C_{11}, C_{12} and C_{44} as a function of the plane-wave energy cutoff (a) and k mesh (b). The energy cutoff convergence (left) is studied keeping the k-points fixed to 20×20×20. The k mesh convergence (right) is studied keeping an energy cutoff of 80 Ry.

to 60 Ry and allowing the k-points sample to change. Only small variations of less than 0.03% (for $\langle 1\,1\,1\rangle\{\bar{1}\,1\,0\}$) and 0.01% (for $\langle 1\,1\,1\rangle\{1\,1\,\bar{2}\}$) were found when comparing the results between a 28×28×1 and a 30×30×1 grid. As such, we chose the 28×28×1 k-point mesh as a good compromise between computational accuracy and computational cost for

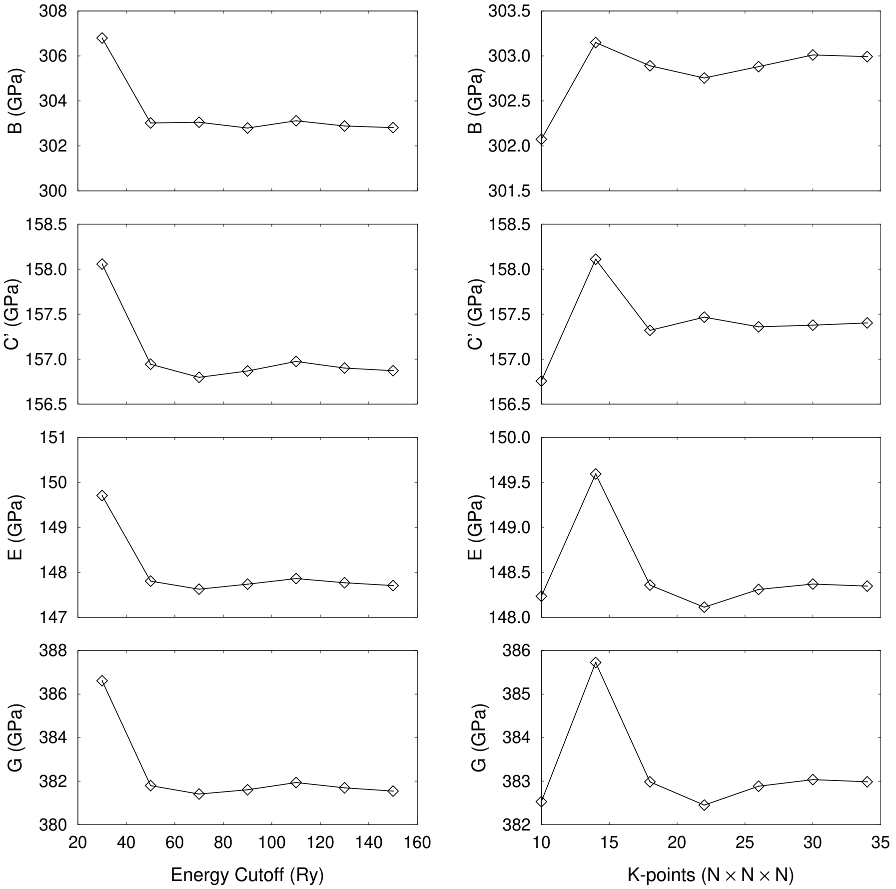

(a) (b)

Figure 10. Convergence of the bulk modulus B, the tetragonal shear elastic constant C', the shear modulus G, and the Young's modulus E as a function of the plane-wave energy cutoff (a) and k mesh (b). The energy cutoff convergence (left) is studied keeping the k-points fixed to 20×20×20. The k mesh convergence (right) is studied keeping an energy cutoff of 80 Ry.

both slip systems. Then we fixed the energy cutoff to 40 Ry and the k points sampling to a 28×28×1 grid, allowing the slab size to change. Previous works in the literature (cf. Table III) have shown that γ_{us} for the $\langle 1\,1\,1\rangle\{1\,1\,\overline{2}\}$ slip system is higher than its counterpart for the $\langle 1\,1\,1\rangle\{\overline{1}\,1\,0\}$ slip system. This trend appears at 12 layers in Fig. A.11(c). Given the significant computational increase of choosing 14 layers instead of 12 layers shown in Fig. A.11(d), we decided to chose a slab size of 12 layers in our simulations.

These convergence tests and the selection of accurate but reasonable DFT parameters are relevant to our approach given the significant computational cost of the first-principles simulations performed to obtain the GSFE along the entire $\langle 1\,1\,1\rangle$ path for each of chemical compositions at each the irradiation time.

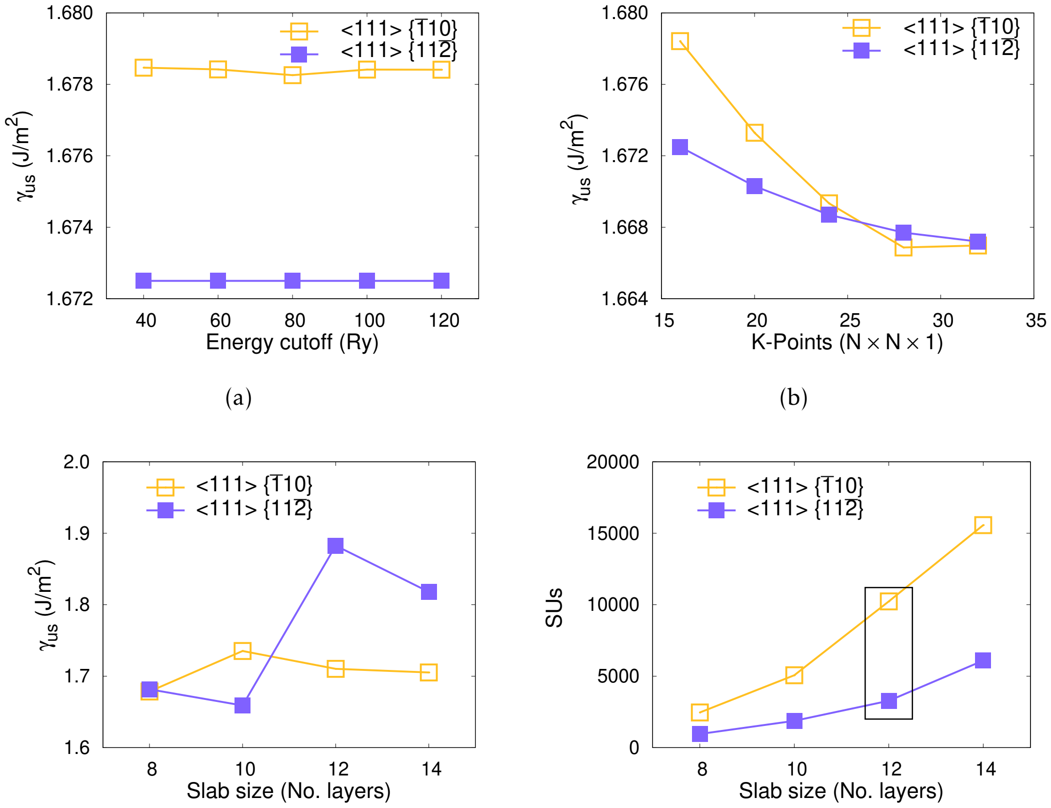

(a)

(b)

(c)

(d)

Figure 11. Benchmarking to identify the set of parameters that guarantee accurate and efficient DFT calculations of the unstable stacking fault energy γ_{us} for transmuted tungsten. Fig. 11(a), 11(b), and 11(c) show the convergence with the energy cutoff, k-points sampling, and slab size, respectively. Fig. 11(d) shows the total number of SUs needed to complete each simulation. The highlighted region in Fig. 11(d) indicates the total number of SUs for the final set of parameters.

---

[1] E. Lassner and S. Wolf-Dieter, Tungsten: Properties, Chemistry, Technology of the Element, Alloys, and Chemica (Springer US, 1999).

[2] H. Bolt, V. Barabash, W. Krauss, J. Linke, R. Neu, S. Suzuki, N. Yoshida, and A. U. Team, Materials for the plasma-facing components of fusion reactors, Journal of nuclear materials **329**, 66 (2004).

[3] A. Giannattasio and S. G. Roberts, Strain-rate dependence of the brittle-to-ductile transition temperature in tungsten, Philosophical Magazine **87**, 2589 (2007).

[4] S. J. Zinkle and N. M. Ghoniem, Prospects for accelerated development of high performance structural materials, Journal of Nuclear Materials **417**, 2 (2011).

[5] M. Rieth, S. Dudarev, S. Gonzalez de Vicente, J. Aktaa, T. Ahlgren, S. Antusch, D. Armstrong, M. Balden, N. Baluc, M.-F. Barthe, et al., Recent progress in research on tungsten materials for nuclear fusion applications in europe, Journal of Nuclear Materials **432**, 482 (2013).

[6] J. F. Dobson, G. Vignale, and M. P. Das, Electronic density functional theory: recent progress and new directions (Springer Science & Business Media, 2013).

[7] W. A. Counts, M. Friak, D. Raabe, and J. Neugebauer, Using ab initio calculations in designing bcc mgli–x alloys for ultra-lightweight applications, Advanced Engineering Materials **12**, 1198 (2010).

[8] D. Roundy, C. Krenn, M. L. Cohen, and J. Morris Jr, The ideal strength of tungsten, Philosophical magazine A **81**, 1725 (2001).

[9] S. Giusepponi and M. Celino, The ideal tensile strength of tungsten and tungsten alloys by first-principles calculations, Journal of nuclear materials **435**, 52 (2013).

[10] C. Yang and L. Qi, Ab initio calculations of ideal strength and lattice instability in w-ta and w-re alloys, Physical Review B **97**, 014107 (2018).

[11] N. Nagasako, M. Jahnátek, R. Asahi, and J. Hafner, Anomalies in the response of v, nb, and ta to tensile and shear loading: Ab initio density functional theory calculations, Physical Review B **81**, 094108 (2010).

[12] Y. Ma, Q.-F. Han, Z.-Y. Zhou, and Y.-L. Liu, First-principles investigation on mechanical behaviors of w-cr/ti binary alloys, Journal of Nuclear Materials **468**, 105 (2016).

[13] X. Li, S. Schönecker, R. Li, X. Li, Y. Wang, J. Zhao, B. Johansson, and L. Vitos, Ab initio calculations of mechanical properties of bcc w–re–os random alloys: effects of transmutation of w, Journal of Physics: Condensed Matter **28**, 295501 (2016).

[14] V. Vitek, Core structure of screw dislocations in body-centred cubic metals: relation to symmetry and interatomic bonding, Philosophical Magazine **84**, 415 (2004).

[15] S. Wurster, B. Gludovatz, and R. Pippan, High temperature fracture experiments on tungsten–rhenium alloys, International Journal of Refractory Metals and Hard Materials **28**, 692 (2010).

[16] H. Li, S. Wurster, C. Motz, L. Romaner, C. Ambrosch-Draxl, and R. Pippan, Dislocation-core symmetry and slip planes in tungsten alloys: Ab initio calculations and microcantilever bending experiments, Acta Materialia **60**, 748 (2012).

[17] G. D. Samolyuk, Y. Osetsky, and R. Stoller, The influence of transition metal solutes on the dislocation core structure and values of the peierls stress and barrier in tungsten, Journal of Physics: Condensed Matter **25**, 025403 (2013).

[18] M. a.-S. Duesbery and V. Vitek, Plastic anisotropy in bcc transition metals, Acta Materialia **46**, 1481 (1998).

[19] K. Ito and V. Vitek, Atomistic study of non-schmid effects in the plastic yielding of bcc metals, Philosophical Magazine A **81**, 1387 (2001).

[20] V. Bulatov, O. Richmond, and M. Glazov, An atomistic dislocation mechanism of pressure-dependent plastic flow in aluminum, Acta materialia **47**, 3507 (1999).

[21] C. Woodward and S. Rao, Ab-initio simulation of isolated screw dislocations in bcc mo and ta, Philosophical Magazine A **81**, 1305 (2001).

[22] R. Gröger and V. Vitek, Breakdown of the schmid law in bcc molybdenum related to the effect of shear stress perpendicular to the slip direction, in Materials Science Forum, Vol. 482 (Trans Tech Publ, 2005) pp. 123–126.

[23] J. Chaussidon, M. Fivel, and D. Rodney, The glide of screw dislocations in bcc fe: atomistic static and dynamic simulations, Acta materialia **54**, 3407 (2006).

[24] M. Gilbert, S. Queyreau, and J. Marian, Stress and temperature dependence of screw dislocation mobility in α-fe by molecular dynamics, Physical Review B **84**, 174103 (2011).

[25] D. Cereceda, M. Diehl, F. Roters, D. Raabe, J. M. Perlado, and J. Marian, Unraveling the temperature dependence of the yield strength in single-crystal tungsten using atomistically-

informed crystal plasticity calculations, International Journal of Plasticity **78**, 242 (2016).

[26] C. Marichal, K. Srivastava, D. Weygand, S. Van Petegem, D. Grolimund, P. Gumbsch, and H. Van Swygenhoven, Origin of anomalous slip in tungsten, Physical review letters **113**, 025501 (2014).

[27] L. Dezerald, D. Rodney, E. Clouet, L. Ventelon, and F. Willaime, Plastic anisotropy and dislocation trajectory in bcc metals, Nature communications **7**, 1 (2016).

[28] A. Kraych, E. Clouet, L. Dezerald, L. Ventelon, F. Willaime, and D. Rodney, Non-glide effects and dislocation core fields in bcc metals, npj Computational Materials **5**, 1 (2019).

[29] J. Marian, C. S. Becquart, C. Domain, S. L. Dudarev, M. R. Gilbert, R. J. Kurtz, D. R. Mason, K. Nordlund, A. E. Sand, L. L. Snead, et al., Recent advances in modeling and simulation of the exposure and response of tungsten to fusion energy conditions, Nuclear Fusion **57**, 092008 (2017).

[30] S. Pugh, Xcii. relations between the elastic moduli and the plastic properties of polycrystalline pure metals, The London, Edinburgh, and Dublin Philosophical Magazine and Journal of Science **45**, 823 (1954).

[31] D. Pettifor, Theoretical predictions of structure and related properties of intermetallics, Materials science and technology **8**, 345 (1992).

[32] D. Suetin, I. Shein, and A. Ivanovskii, Structural, elastic, electronic and magnetic properties of perovskite-like co3wc, rh3wc and ir3wc from first principles calculations, Solid state sciences **12**, 814 (2010).

[33] G. N. Greaves, A. Greer, R. S. Lakes, and T. Rouxel, Poisson's ratio and modern materials, Nature materials **10**, 823 (2011).

[34] J. R. Rice, Dislocation nucleation from a crack tip: an analysis based on the peierls concept, Journal of the Mechanics and Physics of Solids **40**, 239 (1992).

[35] M. Muzyk, D. Nguyen-Manh, K. J. Kurzydłowski, N. L. Baluc, and S. L. Dudarev, Phase stability, point defects, and elastic properties of w-v and w-ta alloys, Phys. Rev. B **84**, 104115 (2011).

[36] M. Muzyk, D. Nguyen-Manh, J. Wróbel, K. Kurzydłowski, N. Baluc, and S. Dudarev, First-principles model for phase stability, radiation defects and elastic properties of w–ta and w–v alloys, Journal of Nuclear Materials **442**, S680 (2013).

[37] N. Wei, T. Jia, X. Zhang, T. Liu, Z. Zeng, and X. Yang, First-principles study of the phase

stability and the mechanical properties of w-ta and w-re alloys, AIP Advances **4**, 057103 (2014).

[38] C.-H. Huang, L. Gharaee, Y. Zhao, P. Erhart, and J. Marian, Mechanism of nucleation and incipient growth of re clusters in irradiated w-re alloys from kinetic monte carlo simulations, Physical Review B **96**, 094108 (2017).

[39] D. Jiang, C. Ouyang, and S. Liu, Mechanical properties of w–ti alloys from first-principles calculations, Fusion Engineering and Design **106**, 34 (2016).

[40] Y.-J. Hu, S.-L. Shang, Y. Wang, K. A. Darling, B. G. Butler, L. J. Kecskes, and Z.-K. Liu, Effects of alloying elements and temperature on the elastic properties of w-based alloys by first-principles calculations, Journal of Alloys and Compounds **671**, 267 (2016).

[41] S. Giusepponi and M. Celino, The ideal tensile strength of tungsten and tungsten alloys by first-principles calculations, Journal of nuclear materials **435**, 52 (2013).

[42] J. Qian, C. Wu, J. Fan, and H. Gong, Effect of alloying elements on stacking fault energy and ductility of tungsten, Journal of Alloys and Compounds **737**, 372 (2018).

[43] T. Suzudo, M. Yamaguchi, and A. Hasegawa, Stability and mobility of rhenium and osmium in tungsten: first principles study, Modelling and Simulation in Materials Science and Engineering **22**, 075006 (2014).

[44] M. Hossain and J. Marian, Stress-dependent solute energetics in w–re alloys from first-principles calculations, Acta materialia **80**, 107 (2014).

[45] L. Gharaee, J. Marian, and P. Erhart, The role of interstitial binding in radiation induced segregation in w-re alloys, Journal of Applied Physics **120**, 025901 (2016).

[46] S. Giusepponi and M. Celino, The effects of vacancies in the mechanical properties of tungsten: A first-principles study, Nuclear Instruments and Methods in Physics Research Section B: Beam Interactions with Materials and Atoms **342**, 70 (2015).

[47] W. Setyawan, G. Nandipati, and R. J. Kurtz, Ab initio study of interstitial cluster interaction with re, os, and ta in w, Journal of Nuclear Materials **484**, 30 (2017).

[48] L. Romaner, C. Ambrosch-Draxl, and R. Pippan, Effect of rhenium on the dislocation core structure in tungsten, Physical review letters **104**, 195503 (2010).

[49] H. Li, S. Wurster, C. Motz, L. Romaner, C. Ambrosch-Draxl, and R. Pippan, Dislocation-core symmetry and slip planes in tungsten alloys: Ab initio calculations and microcantilever bending experiments, Acta materialia **60**, 748 (2012).

[50] X. Wu, Y.-W. You, X.-S. Kong, J.-L. Chen, G.-N. Luo, G.-H. Lu, C. Liu, and Z. Wang, First-principles determination of grain boundary strengthening in tungsten: dependence on grain boundary structure and metallic radius of solute, Acta Materialia **120**, 315 (2016).

[51] J. -Ch. Sublet, J. W. Eastwood, J. G. Morgan, M. R. Gilbert, M. Fleming, and W. Arter, FISPACT-II: An advanced simulation system for activation, transmutation and material modelling, Nucl. Data Sheets **139**, 77 (2017), `http://dx.doi.org/10.1016/j.nds.2017.01.002`.

[52] M. Fleming, T. Stainer, and M. R. Gilbert, The FISPACT-II User Manual, Tech. Rep. UKAEA-R(18)001 (UKAEA, 2018) available from `http://fispact.ukaea.uk`.

[53] U. Fischer, C. Bachmann, J. P. Catalan, T. Eade, D. Flammini, M. Gilbert, J. Jaboulay, A. Konobeev, D. Leichtle, L. Lu, F. Malouch, F. Moro, P. Pereslavtsev, Y. Qiu, J. Sanz, P. Sauvan, G. Stankunas, , A. Travleev, A. Turner, F. Ogando, I. Palermo, and R. Villari., Methodological approach for DEMO neutronics in the European PPPT programme: Tools, data and analyses, Fus. Eng. Des. **123**, 26 (2017).

[54] M. R. Gilbert, T. Eade, C. Bachmann, U. Fischer, and N. P. Taylor, Waste assessment of european demo fusion reactor designs, Fus. Eng. Des. **136**, 42 (2018), `https://doi.org/10.1016/j.fusengdes.2017.12.019`.

[55] G. Federici, R. Kemp, D. Ward, C. Bachmann, T. Franke, S. Gonzalez, C. Lowry, M. Gadomska, J. Harman, B. Meszaros, C. Morlock, F. Romanelli, and R. Wenninger, Overview of eu demo design and r&d activities, Fus. Eng. Des. **89**, 882 (2014), proceedings of the 11th International Symposium on Fusion Nuclear Technology-11 (ISFNT-11) Barcelona, Spain, 15-20 September, 2013.

[56] G. Federici, C. Bachmann, L. Barucca, W. Biel, L. Boccaccini, R. Brown, C. Bustreo, S. Ciattaglia, F. Cismondi, M. Coleman, V. Corato, C. Day, E. Diegele, U. Fischer, T. Franke, C. Gliss, A. Ibarra, R. Kembleton, A. Loving, F. Maviglia, B. Meszaros, G. Pintsuk, N. Taylor, M. Tran, C. Vorpahl, R. Wenninger, and J. You, Demo design activity in europe: Progress and updates, Fus. Eng. Des. **136**, 729 (2018), special Issue: Proceedings of the 13th International Symposium on Fusion Nuclear Technology (ISFNT-13).

[57] M. R. Gilbert, L. W. Packer, J.-C. Sublet, and R. A. Forrest, Inventory simulations under neutron irradiation: Visualization techniques as an aid to materials design, Nuclear Science and Engineering **177**, 291 (2014), `https://doi.org/10.13182/NSE13-76`.

[58] M. R. Gilbert, T. Eade, C. Bachmann, U. Fischer, and N. P. Taylor, Activation, decay heat, and waste classification studies of the European DEMO concept, Nucl. Fus. **57**, 046015 (2017), `https://doi.org/10.1088/1741-4326/aa5bd7`.

[59] A. J. Koning and D. Rochman, TENDL-2017 (2017), release Date: April 25, 2018. Available from `https://tendl.web.psi.ch/tendl_2017/tendl2017.html`.

[60] P. Giannozzi, S. Baroni, N. Bonini, M. Calandra, R. Car, C. Cavazzoni, D. Ceresoli, G. L. Chiarotti, M. Cococcioni, I. Dabo, et al., Quantum espresso: a modular and open-source software project for quantum simulations of materials, Journal of physics: Condensed matter **21**, 395502 (2009).

[61] P. Giannozzi, O. Andreussi, T. Brumme, O. Bunau, M. B. Nardelli, M. Calandra, R. Car, C. Cavazzoni, D. Ceresoli, M. Cococcioni, et al., Advanced capabilities for materials modelling with quantum espresso, Journal of Physics: Condensed Matter **29**, 465901 (2017).

[62] J. P. Perdew, K. Burke, and M. Ernzerhof, Generalized gradient approximation made simple, Physical review letters **77**, 3865 (1996).

[63] D. Hamann, Optimized norm-conserving vanderbilt pseudopotentials, Physical Review B **88**, 085117 (2013).

[64] L. Bellaiche and D. Vanderbilt, Virtual crystal approximation revisited: Application to dielectric and piezoelectric properties of perovskites, Physical Review B **61**, 7877 (2000).

[65] H. J. Monkhorst and J. D. Pack, Special points for brillouin-zone integrations, Physical review B **13**, 5188 (1976).

[66] J. F. Nye et al., Physical properties of crystals: their representation by tensors and matrices (Oxford university press, 1985).

[67] M. Mehl, J. Osburn, D. Papaconstantopoulos, and B. Klein, Structural properties of ordered high-melting-temperature intermetallic alloys from first-principles total-energy calculations, Physical Review B **41**, 10311 (1990).

[68] K. Chen, L. Zhao, and J. S. Tse, Ab initio study of elastic properties of ir and ir 3 x compounds, Journal of applied physics **93**, 2414 (2003).

[69] F. Giustino, Materials modelling using density functional theory: properties and predictions (Oxford University Press, 2014).

[70] R. Hill, The elastic behaviour of a crystalline aggregate, Proceedings of the Physical Society. Section A **65**, 349 (1952).

[71] R. Peierls, The size of a dislocation, Proceedings of the Physical Society **52**, 34 (1940).

[72] F. Nabarro, Dislocations in a simple cubic lattice, Proceedings of the Physical Society **59**, 256 (1947).

[73] M.-C. Marinica, L. Ventelon, M. Gilbert, L. Proville, S. Dudarev, J. Marian, G. Bencteux, and F. Willaime, Interatomic potentials for modelling radiation defects and dislocations in tungsten, Journal of Physics: Condensed Matter **25**, 395502 (2013).

[74] A. Stukowski, D. Cereceda, T. D. Swinburne, and J. Marian, Thermally-activated non-schmid glide of screw dislocations in w using atomistically-informed kinetic monte carlo simulations, International Journal of Plasticity **65**, 108 (2015).

[75] D. Caillard, Kinetics of dislocations in pure fe. part i. in situ straining experiments at room temperature, Acta Materialia **58**, 3493 (2010).

[76] D. Caillard, Kinetics of dislocations in pure fe. part ii. in situ straining experiments at low temperature, Acta Materialia **58**, 3504 (2010).

[77] C. Marichal, H. Van Swygenhoven, S. Van Petegem, and C. Borca, {110} slip with {112} slip traces in bcc tungsten, Scientific reports **3** (2013).

[78] D. Cereceda, A. Stukowski, M. Gilbert, S. Queyreau, L. Ventelon, M. Marinica, J. Perlado, and J. Marian, Assessment of interatomic potentials for atomistic analysis of static and dynamic properties of screw dislocations in w, Journal of Physics: Condensed Matter **25**, 085702 (2013).

[79] C. Carter, R. Balluffi, and S. Allen, Kinetics of materials (2005).

[80] W. Tyson and W. Miller, Surface free energies of solid metals: Estimation from liquid surface tension measurements, Surface Science **62**, 267 (1977).

[81] J. Boettger, Nonconvergence of surface energies obtained from thin-film calculations, Physical Review B **49**, 16798 (1994).

[82] V. Fiorentini and M. Methfessel, Extracting convergent surface energies from slab calculations, Journal of Physics: Condensed Matter **8**, 6525 (1996).

[83] X. Li, S. Schönecker, R. Li, X. Li, Y. Wang, J. Zhao, B. Johansson, and L. Vitos, Ab initio calculations of mechanical properties of bcc w–re–os random alloys: effects of transmutation of w, Journal of Physics: Condensed Matter **28**, 295501 (2016).

[84] L. Romaner, C. Ambrosch-Draxl, and R. Pippan, Effect of rhenium on the dislocation core structure in tungsten, Phys. Rev. Lett. **104**, 195503 (2010).

[85] D. Jiang, Q. Zhou, L. Xue, T. Wang, and J. Hu, First-principles study the phase stability and mechanical properties of binary w-mo alloys, Fusion Engineering and Design **130**, 56 (2018).

[86] Y.-L. Liu, H.-B. Zhou, Y. Zhang, S. Jin, and G.-H. Lu, The ideal tensile strength and deformation behavior of a tungsten single crystal, Nuclear Instruments and Methods in Physics Research Section B: Beam Interactions with Materials and Atoms **267**, 3282 (2009), proceedings of the Ninth International Conference on Computer Simulation of Radiation Effects in Solids.

[87] G. D. Samolyuk, Y. N. Osetsky, and R. E. Stoller, The influence of transition metal solutes on the dislocation core structure and values of the peierls stress and barrier in tungsten, Journal of Physics: Condensed Matter **25**, 025403 (2012).

[88] F. H. Featherston and J. Neighbours, Elastic constants of tantalum, tungsten, and molybdenum, Physical Review **130**, 1324 (1963).

[89] L. Vitos, I. Abrikosov, and B. Johansson, Anisotropic lattice distortions in random alloys from first-principles theory-art. no. 156401, PHYSICAL REVIEW LETTERS **8715**, 6401 (2001).

[90] Y.-H. Li, H.-B. Zhou, L. Liang, N. Gao, H. Deng, F. Gao, G. Lu, and G.-H. Lu, Transition from ductilizing to hardening in tungsten: The dependence on rhenium distribution, Acta Materialia **181**, 110 (2019).

[91] G. Bonny, D. Terentyev, A. Bakaev, P. Grigorev, and D. Van Neck, Many-body central force potentials for tungsten, Modelling and Simulation in Materials Science and Engineering **22**, 053001 (2014).

[92] W. Andreoni and A. Curioni, New advances in chemistry and materials science with cpmd and parallel computing, Parallel Computing **26**, 819 (2000).

[93] S. Goedecker, M. Teter, and J. Hutter, Separable dual-space gaussian pseudopotentials, Phys. Rev. B **54**, 1703 (1996).

[94] R. Ayres, G. Shannette, and D. Stein, Elastic constants of tungsten- rhenium alloys from 77 to 298 k, Journal of Applied Physics **46**, 1526 (1975).

[95] Y.-H. Li, H.-B. Zhou, L. Liang, N. Gao, H. Deng, F. Gao, G. Lu, and G.-H. Lu, Transition from ductilizing to hardening in tungsten: The dependence on rhenium distribution, Acta Materialia **181**, 110 (2019).

[96] S. Wurster, N. Baluc, M. Battabyal, T. Crosby, J. Du, C. García-Rosales, A. Hasegawa, A. Hoffmann, A. Kimura, H. Kurishita, et al., Recent progress in r&d on tungsten alloys for divertor structural and plasma facing materials, Journal of Nuclear Materials **442**, S181 (2013).

[97] N. E. Singh-Miller and N. Marzari, Surface energies, work functions, and surface relaxations of low-index metallic surfaces from first principles, Physical Review B **80**, 235407 (2009).

[98] M. Gilbert and J.-C. Sublet, Neutron-induced transmutation effects in w and w-alloys in a fusion environment, Nuclear Fusion **51**, 043005 (2011).

[99] M. R. Gilbert and J. -Ch. Sublet, Scoping of material response under DEMO neutron irradiation: Comparison with fission and influence of nuclear library selection, Fus. Eng. Des. **125**, 299 (2017), `https://doi.org/10.1016/j.fusengdes.2017.06.016`.

[100] F. Hofmann, D. R. Mason, J. K. Eliason, A. A. Maznev, K. A. Nelson, and S. L. Dudarev, Non-contact measurement of thermal diffusivity in ion-implanted nuclear materials, Scientific Reports **5**, 16042 (2015).

[101] M. R. Gilbert, O. Vilkhivskaya, and J. -Ch. Sublet, Fusion decay heat validation, FISPACT-II & TENDL-2019, ENDF/B-VIII.0, JEFF-3.3, EAF2010, and IRDFF-II nu Tech. Rep. UKAEA-CCFE-RE(20)04 (UKAEA, 2020) available from `http://fispact.ukaea.uk`.

[102] M. R. Gilbert and J. Sublet, Experimental decay-heat simulation-benchmark for 14 MeV neutrons & complex inventory analysis with FISPACT-II, Nucl. Fus. **59**, 086045 (2019).

[103] MCNP6 user manual, version 2.0 (2017), edited by C.J. Werner, Los Alamos document number: LA-UR-17-29981, Rev. 0. Further details at `http://mcnp.lanl.gov/`.

[104] H. Li, C. Draxl, S. Wurster, R. Pippan, and L. Romaner, Impact of d-band filling on the dislocation properties of bcc transition metals: The case of tantalum-tungsten alloys investigated by density-functional theory, Phys. Rev. B **95**, 094114 (2017).

[105] H. A. Jahn and E. Teller, Stability of polyatomic molecules in degenerate electronic states i orbital degeneracy, Proceedings of the Royal Society of London. Series A-Mathematical and Physical Sciences **161**, 220 (1937).

[106] A. Luo, D. Jacobson, and K. Shin, Solution softening mechanism of iridium and rhenium in tungsten at room temperature, International Journal of Refractory Metals and Hard Materials **10**, 107 (1991).

[107] L. Qi and D. Chrzan, Tuning ideal tensile strengths and intrinsic ductility of bcc refractory

alloys, Physical review letters **112**, 115503 (2014).

[108] Q. Wang, G. Du, N. Chen, C. Jiang, and L. Chen, Ideal strengths and thermodynamic properties of w and w-re alloys from first-principles calculation, Fusion Engineering and Design **155**, 111579 (2020).

[109] D. Ali, N. Mushtaq, and M. Butt, Investigation of active slip-systems in some body-centered cubic metals, Journal of materials science **46**, 3812 (2011).

[110] O. El-Atwani, N. Li, M. Li, A. Devaraj, J. Baldwin, M. M. Schneider, D. Sobieraj, J. S. Wróbel, D. Nguyen-Manh, S. A. Maloy, et al., Outstanding radiation resistance of tungsten-based high-entropy alloys, Science advances **5**, eaav2002 (2019).